SOFT ROBOTICS
Volume 00, Number 00, 2020

DOI: 10.1089/soro.2020.0039

SoRo
Soft Robotics

Analytical Modeling and Design of Generalized Pneu-Net Soft Actuators with Three-Dimensional Deformations

Guoying Gu,[1,2] Dong Wang,[1] Lisen Ge,[1] and Xiangyang Zhu[1,2]

Abstract

Pneu-net soft actuators, consisting of pneumatic networks of small chambers embedded in elastomeric structures, are particularly promising candidates in the society of soft robotics. However, there are few studies on the analytical modeling of pneu-net soft actuators, especially in the three-dimensional space. In this article, based on the minimum potential energy method and the continuum rod theory, we propose an analytical model and corresponding design approach for a class of generalized pneu-net soft actuators (gPNSAs) with both bending and twisting deformations by combining the geometric complexity and material elasticity. We experimentally verify our modeling approach and finally investigate the effects of geometric parameters, material properties, and external force on the deformations of gPNSAs, which can be used as a tool for the design of gPNSAs. We further demonstrate that our developed model can predict the deformations of gPNSAs made of multiple materials.

Keywords: generalized pneu-net soft actuators, analytical modeling, minimum potential energy method, continuum rod theory, soft robotics

Introduction

Soft robots, different from conventional robots made of rigid materials for repetitive works with fine accuracies, are exclusively composed of soft materials that have embodied intelligence and impedance compliance.[1–4] This unique feature makes them capable of changing their shapes or sizes to adapt to the unknown environment, which is promising in the field of health care, field exploration, and human–robot interaction. During the past decade, many pioneering works on soft robot design have been reported for locomotion,[5–7] swimming,[8,9] manipulating,[10–13] and grasping.[14–16]

In these developments, soft materials (with moduli in the order of 10^3–10^9 Pa) play the critical role because conventional actuation mechanisms (such as motors, gears, and screws) made of rigid materials (with moduli in the order of 10^9–10^{12} Pa) lack the compliance.[1–4,17] Although the tendon-driven mechanism with external motors[18] and the series elastic actuation[19,20] provide the possible selections for compliant human–robot interactions, such developed robots are generally made of rigid materials and not real soft bodies. The commonly used soft materials include elastomeric materials,[21–24] shape memory alloys/polymers,[6,12] electroactive polymers,[3,25] and hydrogels.[26,27] Under diverse physical stimuli, such as compressed air, temperature, humidity, voltage, pH, and light, they can be used for soft actuation. Among them, pneumatic soft actuators (also referred to fluidic elastomer actuators or elastic inflatable actuators) are popular in applications owing to their advantages of lightweight, safety, low cost, and easy fabrication.[22–24]

In general, the pneumatic soft actuator consists of an anisotropic elastomer structure with embedded chambers. Upon the pressurized fluid (air or liquid), this anisotropic structure causes the soft actuator to extend, contract, bend, or twist.[23,24] Depending on the different anisotropic structures, pneumatic soft actuators can be generally divided into two categories: fiber-reinforced pneumatic soft actuators and pneu-net (pneumatic-network) soft actuators. The fiber-reinforced pneumatic soft actuators are generally composed of a monolithic hollow elastomer chamber, helically reinforced with a network of fibers.[28,29] Investigation of this kind of pneumatic soft actuators can date back to the McKibben artificial muscles.[30,31] Alternatively, pneu-net soft actuators are a new type of highly extensible soft actuator with pneumatic networks of

[1]Robotics Institute, School of Mechanical Engineering, Shanghai Jiao Tong University, Shanghai, China.
[2]State Key Laboratory of Mechanical System and Vibration, Shanghai Jiao Tong University, Shanghai, China.

small channels embedded in elastomeric structures.[32,33] Recently, many novel and interesting soft robotic systems with these pneumatic soft actuators have been developed,[34–44] which may refer to the recent survey articles[22–24] for a more comprehensive review.

Despite the diverse achievements, the design and modeling of the pneumatic soft actuators usually rely on empirical methods. While the finite element (FE) solvers[45] are commonly used to verify the development and analyze the actuator performance, the development of analytical modeling approaches for pneumatic soft actuators is of importance.[46–48]

Recently, several pioneering works on analytical modeling of fiber-reinforced pneumatic soft actuators have been reported.[28,29,49–51] However, they cannot be applied for the pneu-net soft actuators. Unfortunately, there are few studies on establishing an analytical model for pneu-net soft actuators. By mapping the actuation space to the bending configuration, Alici *et al.*[52] developed a constant curvature model to estimate the quasi-static bending displacement of pneu-net soft actuators. However, this model can still be treated as a kind of gray-box model, only considering the geometry of the actuators and neglecting the elastic behaviors of the soft materials.

For the nonconstant curvature configuration, de Payrebrune and O'Reilly[53] attempted to use a linear, elastic, rod-based constitutive model to capture the bending movement of the pneu-net soft actuators, which well predicted the curvature and radius of the bending deformation of the actuators. However, the existing models are usually developed to characterize the in-plane bending motion without the three-dimensional (3D) motion.

Inspired from the nature (such as the vine plant and elephant trunk) with helical 3D deformations, we have designed and fabricated a generalized pneu-net soft actuator (gPNSA) with oblique chambers that can generate both bending and twisting motions in the 3D space, as shown in Figure 1.[54]

In this article, we propose an analytical model and corresponding design approach for this kind of gPNSAs based on the minimum potential energy method and the continuum rod theory. Different from the pure geometric models, our constitutive model takes both the geometric complexity and the material elasticity into consideration. To verify the development, we fabricate several gPNSAs and build an experimental platform for testing. Comparisons between the theoretical and experimental data show that the predictions of our developed model agree well with the experimental results of gPNSAs in the 3D space.

With the developed model, we further investigate the effects of material properties and geometric parameters on the deformations of gPNSAs. Comparative results demonstrate that our analytical model can be applied to predict the deformations of new gPNSAs with different geometric parameters and even multiple materials. To the best of our knowledge, this is the first time to develop an analytical modeling approach for characterization and prediction of the 3D deformations in pneu-net soft actuators, which can also be used for design.

The remainder of this article is organized as follows. The Design and Fabrication section briefly presents the design and fabrication of the gPNSAs. The Constitutive Modeling section provides the analytical modeling approach for gPNSAs, and the Model Verification section experimentally verifies the developed model. Finally, the Model Analysis and Prediction for Design section presents the results of the model analysis and prediction for design, and the Conclusion section concludes this article.

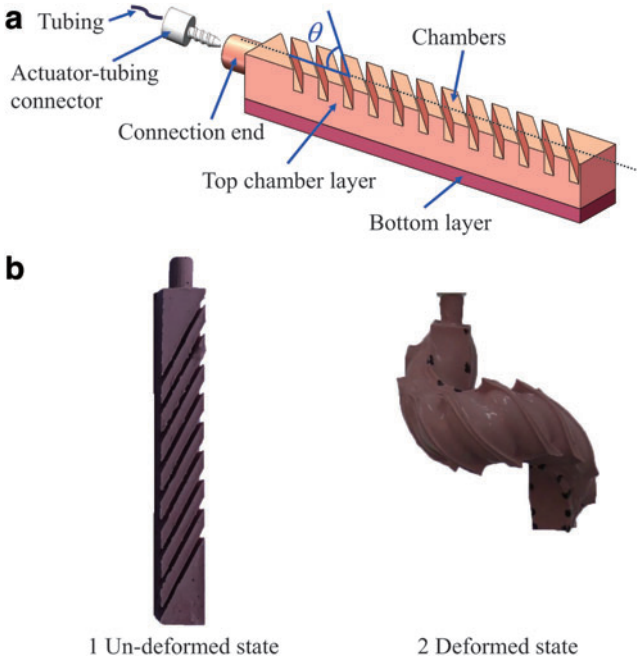

FIG. 1. Schematic illustration of a gPNSA. **(a)** The components of a gPNSA. **(b)** A gPNSA in the undeformed state and deformed state. gPNSA, generalized pneu-net soft actuator. Color images are available online.

Design and Fabrication

Figure 1a shows the schematic structure of our designed gPNSA with the oblique angle of θ, which consists of a top chamber layer and a bottom layer. The top chamber layer of the gPNSA contains a group of linearly arranged chambers connected by an internal channel and a cylindrical connection end for the pneumatic tubing. By tuning the chamber angle of θ (Fig. 1a), our gPNSA can achieve coupled bending and twisting deformations when a pressure is supplied (Fig. 1b) at the deformed state. The connection end serves to form a mechanical connection between the chambers and the pneumatic tubing. In addition, the bottom layer of the gPNSA is made of much less compliant elastomers by comparing to the elastomers in the top layer. In this sense, it can be torn or separated from the actuator body when the gPNSA generates more sophisticated coupled bending and twisting motions.

To fabricate the gPNSA, we also use the multistep molding approach,[54,55] which contains the following three steps:

(1) Casting the top chamber layer and bottom layer of the gPNSA;
(2) Assembling the top chamber layer and bottom layer to form the complete structure of the gPNSA;
(3) Screwing the actuator-tubing connector into the connection end of the gPNSA for pressure supply.

In this work, both the molds for the gPNSAs and the male stud push-in fit pneumatic fittings are 3D printed. Commercial silicone elastomers (Elastosil M4601 [Wacker] and

Ecoflex 00-30 [Smooth-On]) are used to cast the top chamber layer and bottom layer of the gPNSAs. To fabricate the top chamber layer and bottom layer, the elastomers are mixed, defoamed, and injected into the molds. The filled molds are placed in the oven at 70°C to cure the elastomers. After demolding, the top surface of the bottom layer is evenly coated with the mixed liquid-state elastomer. The top chamber layer is then placed on the bottom layer and the space between them is filled with the mixed liquid-state elastomer. The two layers are placed in the oven at 70°C until cured.

After curing, the complete structure of the gPNSA is fabricated, while the gPNSA is fully enclosed. For inflation, the connection end of the gPNSA is pierced with a needle to form a thorough air channel. The actuator-tubing connector is finally screwed into the connection end of the gPNSA for pressure supply. More details about the fabrication process can be found in Ge's results.[55] In addition, the 3D printing method has been presented to fabricate this kind of gPNSA.[56]

Constitutive Modeling

In this section, we present the constitutive modeling approach for a gPNSA. The equilibrium state is first obtained based on the minimum potential energy method as introduced in the Calculation of the Potential Energy section. We then calculate the elastic energy stored in the gPNSA and the potential energy of force in the Calculation of Elastic Energy W_m section and the Calculation of the Potential Energy of Force W_F section, respectively. Minimization of the total potential energy is given in the Calculation of the Minimum Potential Energy section. In the Model of gPNSAs in the Global Coordinate section, the deformation of gPNSA in the global coordinate system is obtained based on the continuum rod theory.

Calculation of the potential energy

In a gPNSA with n chambers (Fig. 2a), the total potential energy Π can be expressed by

$$\Pi = n \times (W_m - W_F), \tag{1}$$

where W_m and W_F are, respectively, the elastic energy stored in the silicone elastomers and the work done by the supplied pressure in each chamber, and n is the number of chambers.

For each chamber with four parts as shown in Figure 2b, we can calculate W_m as

$$W_m = W_{m1} + W_{m2} + W_{m3} + W_{m4}, \tag{2}$$

where W_{m1}, W_{m2}, W_{m3}, and W_{m4} are the elastic energies in Part 1, Part 2, Part 3, and Part 4, respectively. According to the theory of linear elasticity,[57,58] the strain energy density function per unit volume can be expressed as

$$W_s = \frac{1}{2}\frac{E}{1+v} J_2 + \frac{Ev(1-2v)}{1+v} {J_1}^2, \tag{3}$$

where J_1 and J_2 are the first and second strain invariants, respectively, E and v are the Young modulus and Poisson ratio of the elastomer. Therefore, we can calculate W_{m1}, W_{m2}, W_{m3}, and W_{m4} by

$$\begin{cases} W_{m1} = w \times 2 \times (t_1 + t_2 + t_3) \int_{x_3 = 0}^{h_1} W_s dx_3 \\ W_{m2} = w \times 2 \times (t_1 + t_2) \int_{x_3 = h_1 + h_2}^{h_1 + h_2 + h_5} W_s dx_3 \\ W_{m3} = w \times 2 \times t_2 \int_{x_3 = h_1 + h_2 + h_5}^{h_1 + h_2 + h_3} W_s dx_3 \\ W_{m4} = w \times 2 \times (t_2 + t_3) \int_{x_3 = h_1 + h_2 + h_3}^{h_1 + h_2 + h_3 + h_4} W_s dx_3 \end{cases}, \tag{4}$$

where w is the chamber inner width, which equals the actuator width w_o minus the thickness of the two side walls of the gPNSA. In this work, the side wall thickness of the gPNSAs is set to be 2 mm. t_1, t_2, and t_3 are half of the distances between chambers, inside wall thickness, and half of the chamber inner length, respectively.

Calculation of elastic energy W_m

To facilitate the calculation, we first define four coordinate systems for the gPNSA, including the global coordinate X_1–X_2–X_3, local coordinate x_1–x_2–x_3, chamber orientation coordinate m_1–m_2–m_3, and principal strain coordinate r_1–r_2–r_3, which are shown in Figure 2c.

In the global coordinate X_1–X_2–X_3, the X_1, X_2, X_3 axes are set along with the actuator's length, width, and thickness directions, respectively, and the origin is set on the center point of the bottom surface. At the undeformed state (Fig. 2c–1), the local reference frame x_1–x_2–x_3 coincides with the global coordinate. However, it will be changed following the deformation of the gPNSA at the deformed state (Fig. 2c–2).

In the chamber orientation coordinate m_1–m_2–m_3, the m_1 axis rotates from the x_1 axis by the chamber orientation angle θ about the m_3 axis. In this work, we assume that the bending and twisting motions of the gPNSA can be represented by a helical rod with the pitch P_t and radius R, which will be verified in the following experiments. In this sense, we can set the r_3 axis in the principal strain coordinate coincides with the x_3 axis and the r_1 axis rotates counterclockwise from the x_1 axis in the same plane by an unknown parameter ϕ, which results in zero shear deformation in the r_1–r_2 principal strain plane. Therefore, in the principal strain coordinate r_1–r_2–r_3, the strain only has three principal components. We define the three principal components at $x_3 = 0$ as e_{11}, e_{22}, and e_{33}. Next, we define the bending curvatures of the gPNSA along the r_1 and r_2 axes with curvatures κ_1 and κ_2, respectively.

Based on Euler–Bernoulli beam theory, we can calculate the strain $\varepsilon^{(r)}$in the principal strain coordinate r_1–r_2–r_3 by

$$\left[\varepsilon^{(r)}\right] = \begin{pmatrix} \varepsilon_{11}^{(r)} & 0 & 0 \\ 0 & \varepsilon_{22}^{(r)} & 0 \\ 0 & 0 & \varepsilon_{33}^{(r)} \end{pmatrix}, \tag{5}$$

where $\varepsilon_{11}^{(r)} = e_{11} + x_3\kappa_1$, $\varepsilon_{22}^{(r)} = e_{22} + x_3\kappa_2$, and $\varepsilon_{33}^{(r)} = e_{33} + x_3 q$. Here, q denotes the gradient of the strain component along the x_3 axis, which is required for plane strain compatibility.[59,60]

Thus, the strain invariants in Equation (3) can be represented by[61]

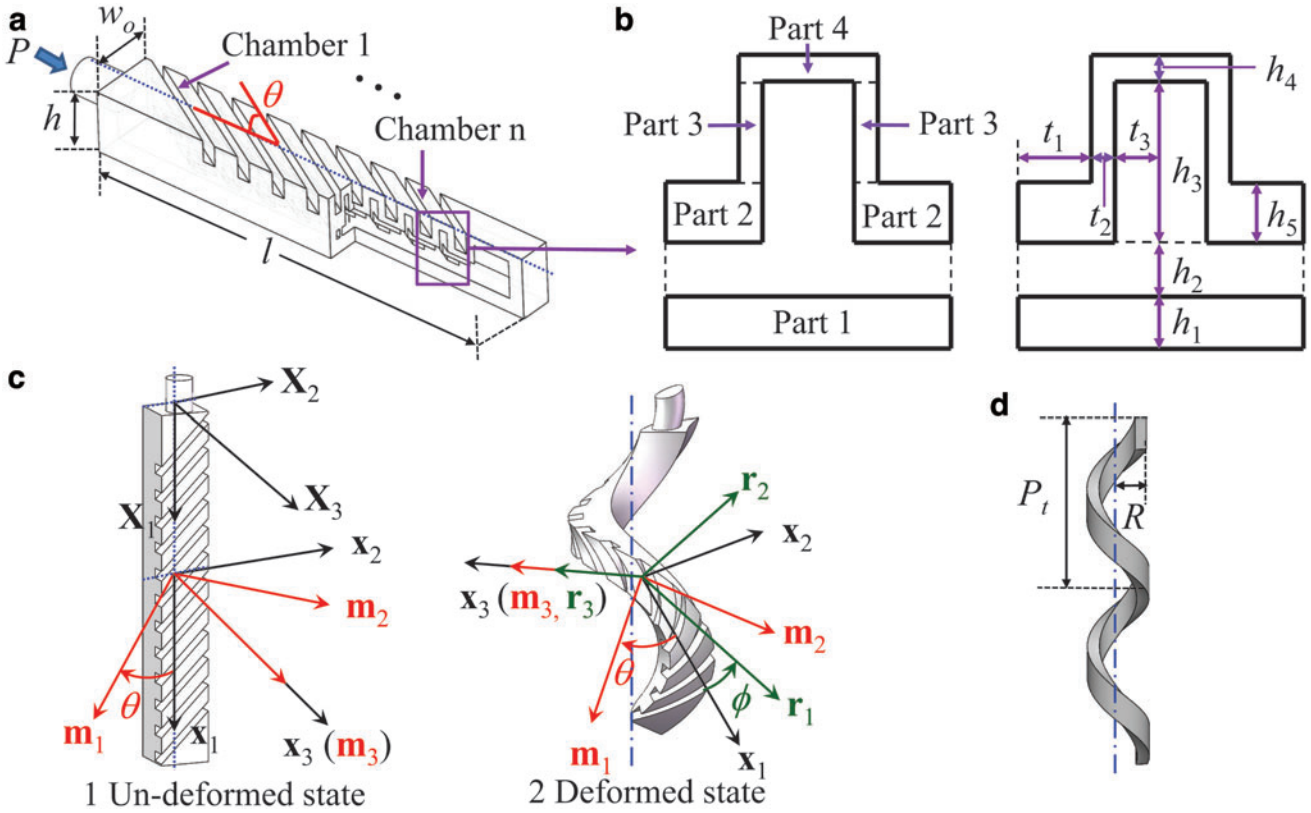

FIG. 2. Schematic illustration of the dimensions and deformations of a gPNSA. **(a)** The gPNSA with length l, width w_o, height h, chamber angle θ, and chamber number n. **(b)** Each chamber of the gPNSA is divided into Part 1, Part 2, Part 3, and Part 4. The labeled geometrical parameters for each chamber are demonstrated. **(c)** The coordinate systems of the gPNSA at the undeformed state and deformed state. **(d)** The deformation of centerline of the gPNSA is characterized with a helical rod with the pitch P_t and radius R. Color images are available online.

$$\begin{cases} J_1 = \varepsilon_{11}^{(r)} + \varepsilon_{22}^{(r)} + \varepsilon_{33}^{(r)} \\ J_2 = \left(\varepsilon_{11}^{(r)}\right)^2 + \left(\varepsilon_{22}^{(r)}\right)^2 + \left(\varepsilon_{33}^{(r)}\right)^2 \end{cases} \tag{6}$$

By further substituting Equations (6) and (11) into Equations (3) and (4), we can calculate the elastic energy W_m by Equation (2).

Calculation of the potential energy of force W_F

According to Equation (5), the strain $\varepsilon^{(m)}$in chamber orientation coordinate m_1–m_2–m_3 can be obtained by

$$\begin{aligned} \left[\varepsilon^{(m)}\right] &= [Q]^T \left[\varepsilon^{(r)}\right][Q] \\ &= \begin{bmatrix} \varepsilon_{11}^{(r)}\cos^2(\theta-\phi) + \varepsilon_{22}^{(r)}\sin^2(\theta-\phi) & \left(\varepsilon_{22}^{(r)} - \varepsilon_{11}^{(r)}\right)\times\cos(\theta-\phi)\times\sin(\theta-\phi) & 0 \\ \left(\varepsilon_{22}^{(r)} - \varepsilon_{11}^{(r)}\right)\times\cos(\theta-\phi)\times\sin(\theta-\phi) & \varepsilon_{11}^{(r)}\sin^2(\theta-\phi) + \varepsilon_{22}^{(r)}\cos^2(\theta-\phi) & 0 \\ 0 & 0 & \varepsilon_{33}^{(r)} \end{bmatrix}, \end{aligned} \tag{7}$$

where $Q = \begin{bmatrix} \cos(\theta-\phi) & -\sin(\theta-\phi) & 0 \\ \sin(\theta-\phi) & \cos(\theta-\phi) & 0 \\ 0 & 0 & 1 \end{bmatrix}$ represents the transformation matrix that rotates the basic vectors r_1–r_2–r_3 into m_1–m_2–m_3 by an angle θ–ϕ around the x_3 axis in the counterclockwise direction.

At the deformed state, when a pressure P is supplied to the gPNSA, the potential energy of force W_F in each chamber is calculated by

$$W_F = P \times \Delta V, \tag{8}$$

where ΔV is the volume change. Due to the geometrical inconsistency at the front and the end of the gPNSA, the complex inner structure, the helical deformation, and possible contact between the chambers, the exact amount of the volume change is generally difficult to be obtained. Considering the fact that the bending and twisting deformations of a gPNSA are mainly driven by the pressure in the top chambers, we calculate the volume change of the top

chamber in Equation (8) for simplicity. To consider the volume change of other parts, we introduce an effective parameter c, as generally used in the literature.[49,53,62] Therefore, the volume change can be obtained by $\Delta V = c \times h_3 \times \frac{w}{\sin\theta} \times 2t_3\varepsilon_{22}^{(m)}$, where h_3 and $\frac{w}{\sin\theta}$ are the height and width of the chamber, respectively, and $2t_3\varepsilon_{22}^{(m)}$ is the length change in the $\boldsymbol{x}_1$ direction.

Using Equations (7) and (8), the potential energy of force W_F can then be obtained by:

$$\begin{aligned} W_F &= c \times P \times h_3 \times \frac{w}{\sin\theta} \times 2t_3\varepsilon_{22}^{(m)} \\ &= c\frac{2Ph_3wt_3}{\sin\theta}\left[\varepsilon_{11}^{(r)}\sin^2(\theta-\phi) + \varepsilon_{22}^{(r)}\cos^2(\theta-\phi)\right], \end{aligned} \tag{9}$$

where c is fitted based on the theoretical predictions and experimental results.

Calculation of the minimum potential energy

Based on the obtained W_m and W_F, the total potential energy Π in Equation (1) can be further prescribed as a function of seven independent variables in the form of

$$\Pi = \Pi(\kappa_1, \kappa_2, q, e_{11}, e_{22}, e_{33}, \phi). \tag{10}$$

At the condition of equilibrium, the total potential energy is minimum against small changes in the seven independent variables, which indicates

$$\begin{cases} \frac{\partial\Pi}{\partial\kappa_1} = 0 \\ \frac{\partial\Pi}{\partial\kappa_2} = 0 \\ \frac{\partial\Pi}{\partial q} = 0 \\ \frac{\partial\Pi}{\partial e_{11}} = 0 \\ \frac{\partial\Pi}{\partial e_{22}} = 0 \\ \frac{\partial\Pi}{\partial e_{33}} = 0 \\ \frac{\partial\Pi}{\partial\phi} = 0. \end{cases} \tag{11}$$

By solving the seven equations in Equation (11) numerically, the seven independent variables can be obtained.

Model of gPNSAs in the global coordinate

According to the results in Equation (11), we have obtained the constitutive model in the principal strain coordinate r_1–r_2–r_3. Next, we will derive the constitutive model in the global coordinate X_1–X_2–X_3 to further analyze the deformations of the gPNSA in the 3D space.

As shown in Figure 2d, we can use the centerline to represent the deformation of the gPNSA. Based on the continuum rod theory,[63] the points along the centerline can be represented by a vector $\boldsymbol{P}(s)$ in the global coordinate X_1–X_2–X_3 as:

$$\boldsymbol{P} = \boldsymbol{P}(s) = \boldsymbol{X}_1(s)\boldsymbol{X}_1 + \boldsymbol{X}_2(s)\boldsymbol{X}_2 + \boldsymbol{X}_3(s)\boldsymbol{X}_3, \tag{12}$$

where s denotes the arc-length parameter. Since the tangent direction of the centerline coincides with the x_1 direction, we can obtain

$$\frac{d\boldsymbol{P}}{ds} = x_1. \tag{13}$$

According to the coordinate transformation, the relation between r_1–r_2 basis and x_1 basis is

$$\boldsymbol{x}_1 = \boldsymbol{r}_1\cos\phi - \boldsymbol{r}_2\sin\phi. \tag{14}$$

By substituting Equation (14) into Equation (13), we can obtain

$$\frac{d\boldsymbol{P}}{ds} = \boldsymbol{r}_1\cos\phi - \boldsymbol{r}_2\sin\phi. \tag{15}$$

In addition, the changes of $\boldsymbol{r}_1$ and $\boldsymbol{r}_2$ with respect to s can be expressed as

$$\begin{aligned} \frac{d\boldsymbol{r}_1}{ds} &= -\boldsymbol{r}_3\kappa_1\cos\phi \\ \frac{d\boldsymbol{r}_2}{ds} &= -\boldsymbol{r}_3\kappa_2\sin\phi \end{aligned}. \tag{16}$$

Since $\boldsymbol{r}_3 = \boldsymbol{r}_1 \times \boldsymbol{r}_2$, the first- and second-order differentiation of $\boldsymbol{r}_3$ basis with respect to s can be expressed as:

Table 1. Geometrical and Material Parameters for Generalized Pneu-Net Soft Actuators with Different Chamber Angles

Parameters	$\theta = 15°$	$\theta = 30°$	$\theta = 45°$	$\theta = 60°$	$\theta = 75°$	$\theta = 90°$
t_1 (mm)	3	1.5	1.5	1	1	1
t_2 (mm)	3.865	2	1.415	1.155	1.035	1
t_3 (mm)	2.135	1	1.085	0.845	0.965	1
h_1 (mm)	3.5	3.5	3.5	3.5	3.5	3.5
h_2 (mm)	2	2	2	2	2	2
h_3 (mm)	7	7	7	7	7	7
h_4 (mm)	2	2	2	2	2	2
h_5 (mm)	4	4	4	4	4	4
h (mm)	14.5	14.5	14.5	14.5	14.5	14.5
l (mm)	104	104	107	104	104	104
w (mm)	11	11	11	11	11	11
w_o (mm)	15	15	15	15	15	15
n	2	8	11	13	13	15
E (kPa)	M4601: 483.5			Ecoflex 00-30: 125		
v	M4601: 0.499			Ecoflex 00-30: 0.499		

Table 2. Fitting Parameter c for Generalized Pneu-Net Soft Actuators with Different Orientation Angles

θ	15°	30°	45°	60°	75°	90°
c	0.12	1	2.72	3	4	5

$$\begin{aligned}\frac{d\boldsymbol{r}_3}{ds} &= \kappa_1 \cos\phi \boldsymbol{r}_1 - \kappa_2 \sin\phi \boldsymbol{r}_2 \\ \frac{d^2\boldsymbol{r}_3}{ds^2} &= -\left(\kappa_1^2 \cos^2\phi + \kappa_2^2 \sin^2\phi\right)\boldsymbol{r}_3\end{aligned}. \quad (17)$$

To resolve Equation (17), we will use the following two boundary conditions:

(1) $\boldsymbol{r}_3(s=0) = \boldsymbol{X}_3$;

(2) $\frac{d\boldsymbol{r}_3(s=0)}{ds} = \kappa_1 \cos\phi \boldsymbol{r}_1(s=0) - \kappa_2 \sin\phi \boldsymbol{r}_2(s=0)$ with $\boldsymbol{r}_1(s=0) = \cos\phi \boldsymbol{X}_1 + \sin\phi \boldsymbol{X}_2$ and $\boldsymbol{r}_2(s=0) = -\sin\phi \boldsymbol{X}_1 + \cos\phi \boldsymbol{X}_2$.

Then, we can obtain

$$\boldsymbol{r}_3 = \left(\frac{\beta}{\alpha}\sin\alpha s\right)\boldsymbol{X}_1 - \left(\frac{\tau}{\alpha}\sin\alpha s\right)\boldsymbol{X}_2 + (\cos\alpha s)\boldsymbol{X}_3, \quad (18)$$

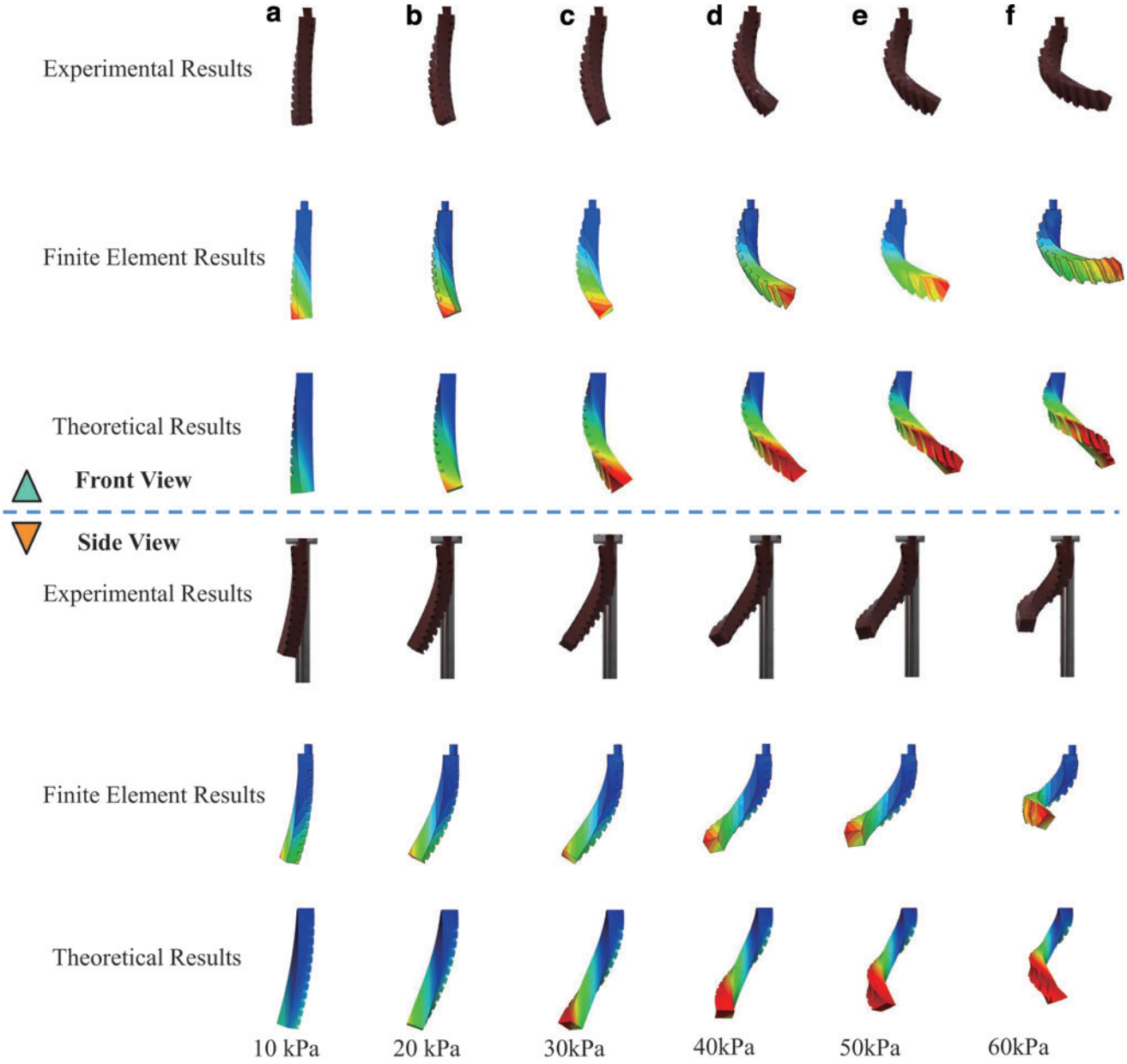

FIG. 3. Experimental, FE simulated, and theoretical results of the deformations of the gPNSA with 45° chamber angle under different supplied pressure P. **(a)** $P = 10$ kPa. **(b)** $P = 20$ kPa. **(c)** $P = 30$ kPa. **(d)** $P = 40$ kPa. **(e)** $P = 50$ kPa. **(f)** $P = 60$ kPa. FE, finite element. Color images are available online.

where $\alpha = \sqrt{\kappa_1^2 \cos^2\phi + \kappa_2^2 \sin^2\phi}$, $\beta = \kappa_1 \cos^2\phi + \kappa_2 \sin^2\phi$, and $\tau = (\kappa_2 - \kappa_1)\sin\phi\cos\phi$.

By substituting Equation (18) into Equation (17) and integrating both sides, $\boldsymbol{r}_1$ and $\boldsymbol{r}_2$ can be calculated by

$$\begin{aligned}\boldsymbol{r}_1 = &\left(\cos\phi + \frac{\beta}{\alpha^2}\kappa_1(\cos\alpha s - 1)\cos\phi\right)\boldsymbol{X}_1 \\ &+ \left(\sin\phi - \frac{\tau}{\alpha^2}\kappa_1(\cos\alpha s - 1)\cos\phi\right)\boldsymbol{X}_2 \\ &- \left(\frac{\kappa_1}{\alpha}\sin\alpha s\cos\phi\right)\boldsymbol{X}_3,\end{aligned} \tag{19}$$

$$\begin{aligned}\boldsymbol{r}_2 = &\left(-\sin\phi - \frac{\beta}{\alpha^2}\kappa_2(\cos\alpha s - 1)\sin\phi\right)\boldsymbol{X}_1 \\ &+ \left(\cos\phi + \frac{\tau}{\alpha^2}\kappa_2(\cos\alpha s - 1)\sin\phi\right)\boldsymbol{X}_2 \\ &+ \left(\frac{\kappa_2}{\alpha}\sin\alpha s\sin\phi\right)\boldsymbol{X}_3.\end{aligned} \tag{20}$$

With Equations (19) and (20), we can integrate Equation (15) to obtain the points $\boldsymbol{P}$ on the centerline as follows:

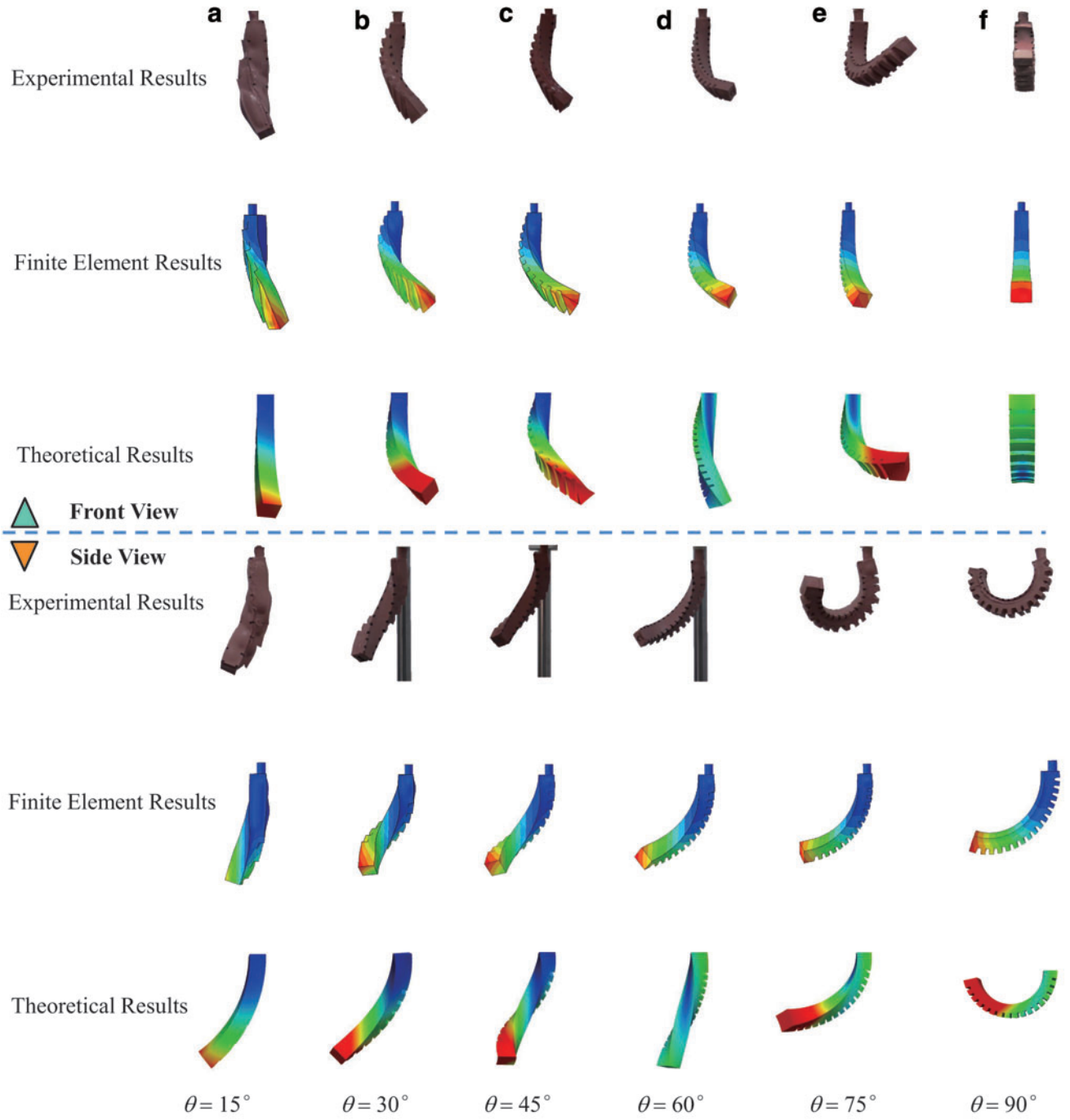

FIG. 4. Experimental, FE simulated, and theoretical results of the deformation of the gPNSAs with different chamber angles when $P = 40$ kPa. **(a)** $\theta = 15°$. **(b)** $\theta = 30°$. **(c)** $\theta = 45°$. **(d)** $\theta = 60°$. **(e)** $\theta = 75°$. **(f)** $\theta = 90°$.Color images are available online. Color images are available online.

$$\boldsymbol{X}_1(s) = s\cos^2\phi - \frac{\kappa_1 s\beta\cos^2\phi}{\alpha^2} + \frac{\kappa_1\beta\cos^2\phi\sin(s\alpha)}{\alpha^3} + s\sin^2\phi - \frac{\kappa_2 s\beta\sin^2\phi}{\alpha^2} + \frac{\kappa_2\beta\sin^2\phi\sin(s\alpha)}{\alpha^3}, \quad (21)$$

$$\boldsymbol{X}_2(s) = \frac{\tau(\kappa_1+\kappa_2+(\kappa_1-\kappa_2)\cos 2\phi)(s\alpha-\sin s\alpha)}{2\alpha^3}, \quad (22)$$

$$\boldsymbol{X}_3(s) = \frac{(\cos s\alpha-1)(\kappa_1+\kappa_2+(\kappa_1-\kappa_2)\cos 2\phi)}{2\alpha^2}. \quad (23)$$

Based on the geometric relation of a helical rod, we can further calculate the pitch P_t and radius R (Fig. 2d) as follows:

$$P_t = \sqrt{\boldsymbol{X}_1\left(s=\frac{2\pi}{\alpha}\right)^2 + \boldsymbol{X}_2\left(s=\frac{2\pi}{\alpha}\right)^2 + \boldsymbol{X}_3\left(s=\frac{2\pi}{\alpha}\right)^2} = \left|2\pi\frac{(\kappa_1-\kappa_2)\sin 2\phi}{\kappa_1^2+\kappa_2^2+(\kappa_1-\kappa_2)(\kappa_1+\kappa_2)\cos 2\phi}\right|, \quad (24)$$

$$R = \frac{\sqrt{\boldsymbol{X}_1\left(s=\frac{\pi}{\alpha}\right)^2 + \boldsymbol{X}_2\left(s=\frac{\pi}{\alpha}\right)^2 + \boldsymbol{X}_3\left(s=\frac{\pi}{\alpha}\right)^2 - (P_t/2)^2}}{2} = \left|\frac{\kappa_1+\kappa_2+(\kappa_1-\kappa_2)\cos 2\phi}{\kappa_1^2+\kappa_2^2+(\kappa_1-\kappa_2)(\kappa_1+\kappa_2)\cos 2\phi}\right|. \quad (25)$$

Model Verification

In this section, the comparative experimental and FE results are presented to verify the effectiveness of our developed constitutive model by changing the supplied pressures and the oblique chamber angles.

In the theoretical predictions, the inputs are the geometrical and material parameters and the applied pressure of the gPNSA. The output is its deformed shape, which is generally characterized by the slope S (or pitch P_t) and curvature κ. The current model is implemented in a MATHEMATICA code, and the coordinates of each point on the gPNSAs are outputted. The deformation is then plotted using ParaView.[64] All model parameters are determined by the material property and geometry of the gPNSA, which are summarized in Table 1. The parameter c is identified in Table 2 for different angle $\theta_0 = 15°$, 30°, 45°, 60°, 75°, and 90°, respectively. Note that the fitted parameter c is the same for one gPNSA with a certain chamber angle and we will not tune it in the following model verification.

Model verification with different supplied pressures P

First, we experimentally verify our model with different supplied pressures P (i.e., $P = 10$, 20, 30, 40, 50, and 60 kPa). The setup and method to measure the deformation of the gPNSA are detailed in our previous work.[54] As an illustration, Figure 3 shows the visual comparison between the experimental, FE simulated, and theoretically predicted deformations of a gPNSA with the chamber angle of 45°. In this figure, both front and side views of the gPNSA are plotted for a clear observation of the bending and twisting deformations in the 3D space.

From the qualitative comparisons, we can see that our model predictions agree well with the experimental results. With the increase of the supplied pressures, there is a little discrepancy at the end of the gPNSA.

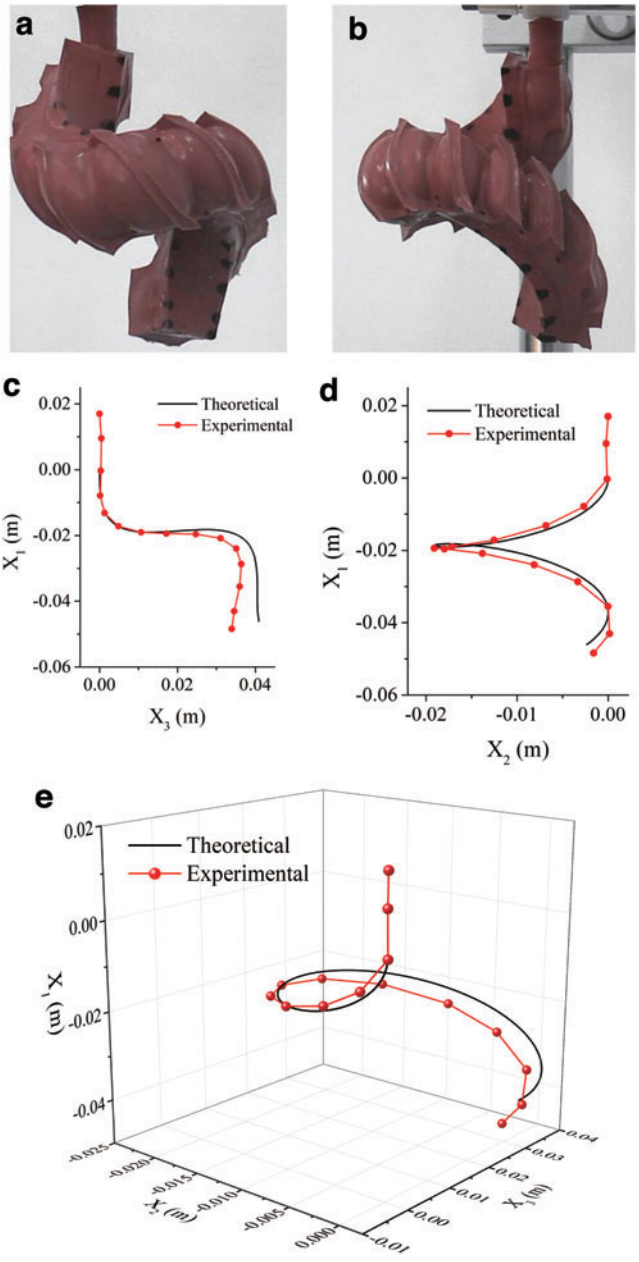

FIG. 5. Determinations of the P_t and radius R by fitting the experimental deformed shape with the parametrization of a helix. Snapshots of gPNSAs with $\theta = 45°$ and $P = 90$ kPa in **(a)** side view and **(b)** front view. The coordinates of the points on the centerline are obtained by the ImageJ. Fittings of the parametrization of the helical function with the obtained experimental points are shown in **(c)** side view and **(d)** front view, respectively. **(e)** The fitting of the obtained points with the parametrization of a helix in 3D (experimental results: *red markers*; model predictions: *black solid curve*). Color images are available online.

Model verification with different chamber angles θ

By varying the chamber angles (i.e., $\theta = 15°$, 30°, 45°, 60°, 75°, and 90°), Figure 4 also shows the visual comparison between experimental, FE simulated, and theoretical predicted deformations of a gPNSA under the supplied pressure of 40 kPa.

It can be seen that with small θ, our model agrees well with the experimental and FE simulated results. However, with a relatively larger θ (such as $\theta = 60°$), FE simulated results predict better than the theoretical results. As θ is around 60°, the gPNSA will mainly twist along its centerline (as will be shown in Fig. 9). Therefore, a large contact force will exist between the chamber and drive the gPNSA to deform, which is neglected by theoretical modeling. With further increase of chamber angles (such as $\theta = 75°$ and 90°), our model predictions agree well with the experimental results, comparing to the FE simulated results.

Quantitative comparisons

In geometry, the curvature mainly characterizes the bending deformation and the pitch describes the out-of-plane twisting motion. For quantitative comparisons between the model predictions and experimental results, we first obtain the experimental curvature (κ) and pitch (P_t) by fitting the experimental coordinates with the parametric form of the helix using the least square method. Next, we compare the obtained experimental κ and P_t with the theoretically predicted values for gPNSAs with various θ and P.

The P_t and κ of the experimental deformed shapes are obtained as explained below. The pixel coordinates of the points on the centerline of a deformed gPNSA in the front and side views are collected by the ImageJ.[65] An example of gPNSAs with $\theta = 45°$ and $P = 90$ kPa is shown in Figure 5a and b. The pixel coordinates are then processed to obtain the real coordinates. The function of a helix with pitch P_t and

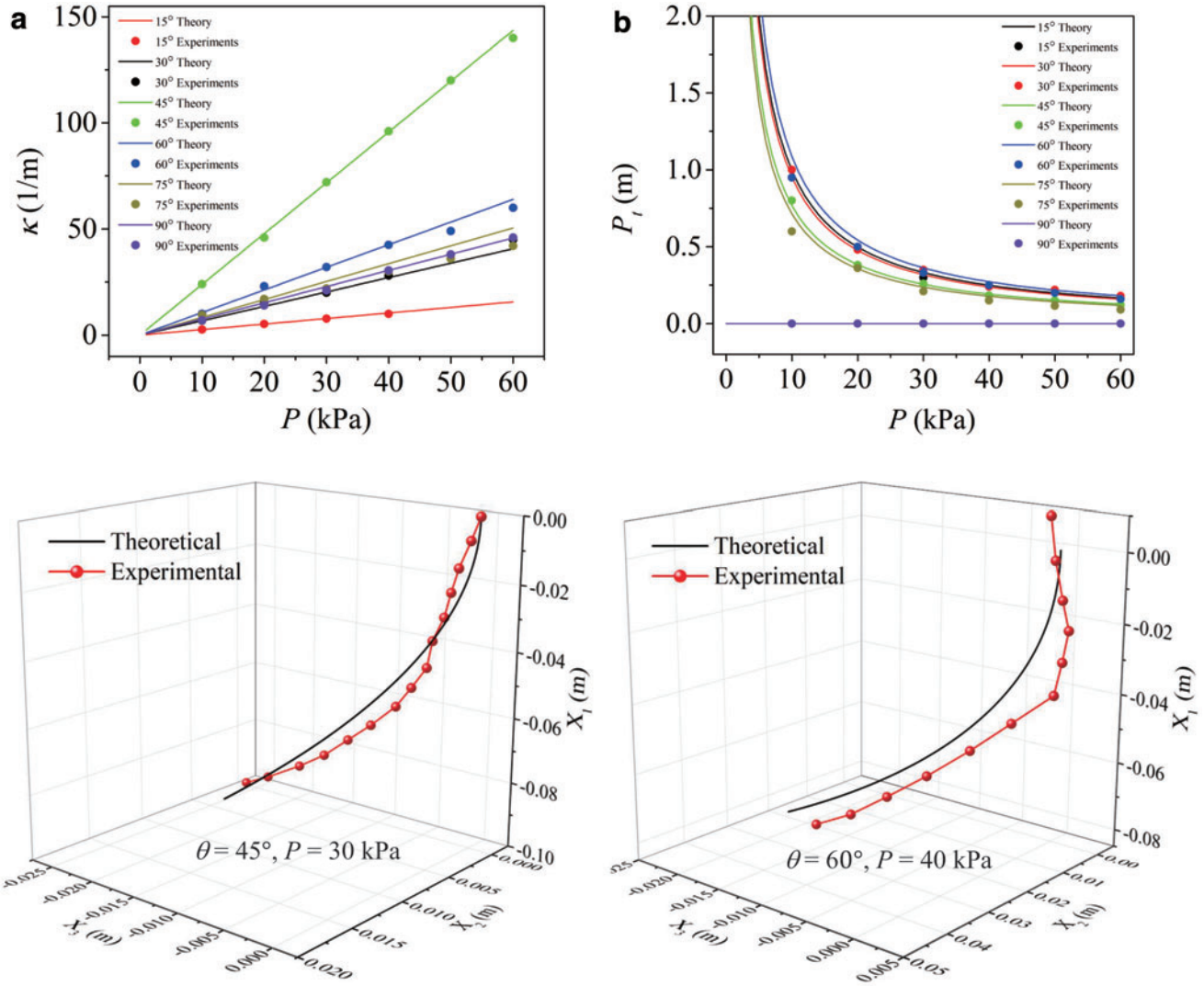

FIG. 6. Validation of the theoretical model. **(a)** κ and **(b)** P_t are plotted as a function of the supplied pressure P for the gPNSAs with different chamber angles (experimental results: *circles*; theoretical results: *solid curves*). Comparison of the theoretical predicted (*black solid curve*) and experimental (*red markers*) space curves of the centerline of the gPNSAs with $\theta = 45°$ and $P = 30$ kPa in **(c)**, and $\theta = 60°$ and $P = 40$ kPa in **(d)**. Color images are available online.

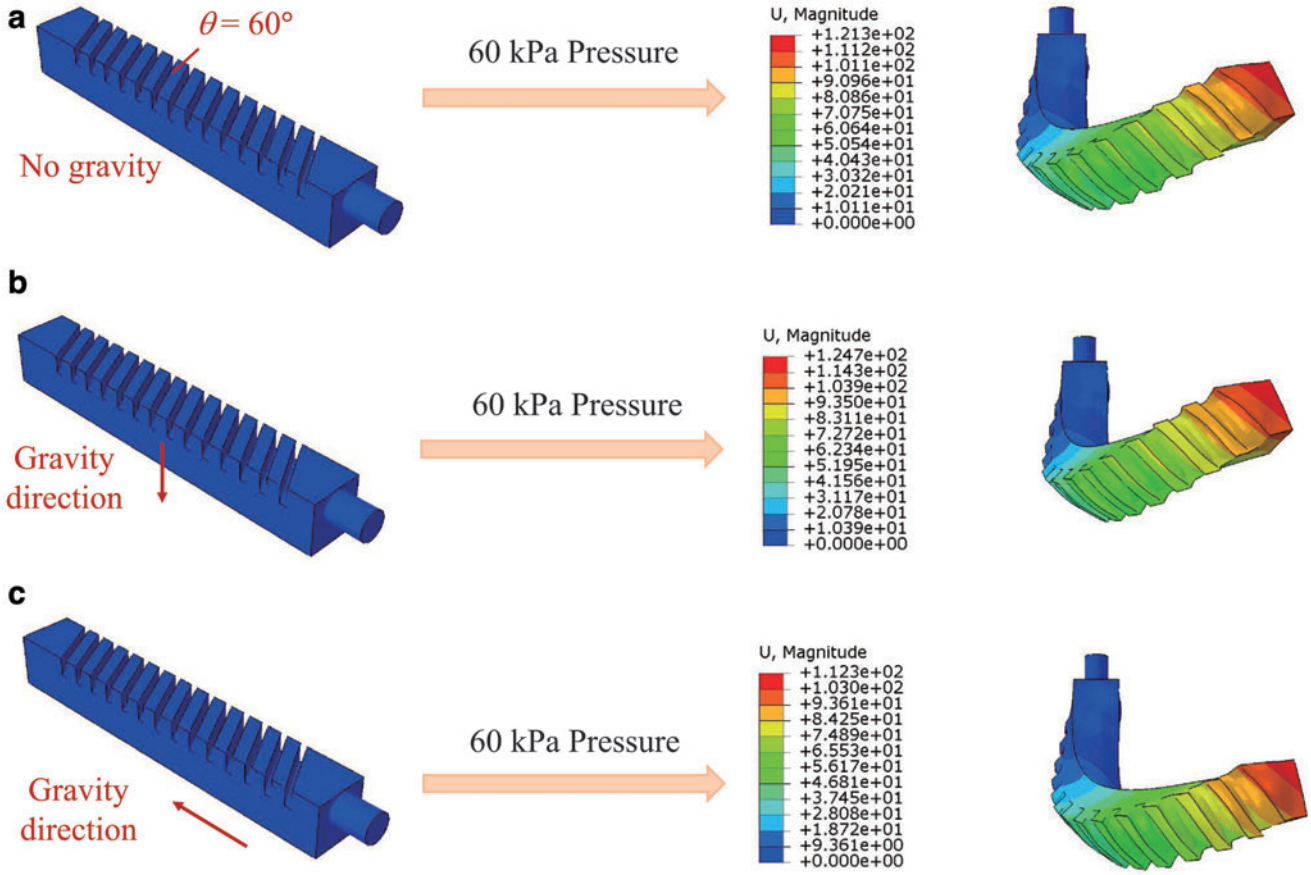

FIG. 7. Effects of the gravity. Undeformed and deformed shapes of the gPNSAs without the gravity **(a)**, with the gravity along the depth direction **(b)**, and the gravity along the length direction **(c)** under the input pressure of $P = 60$ kPa. Color images are available online.

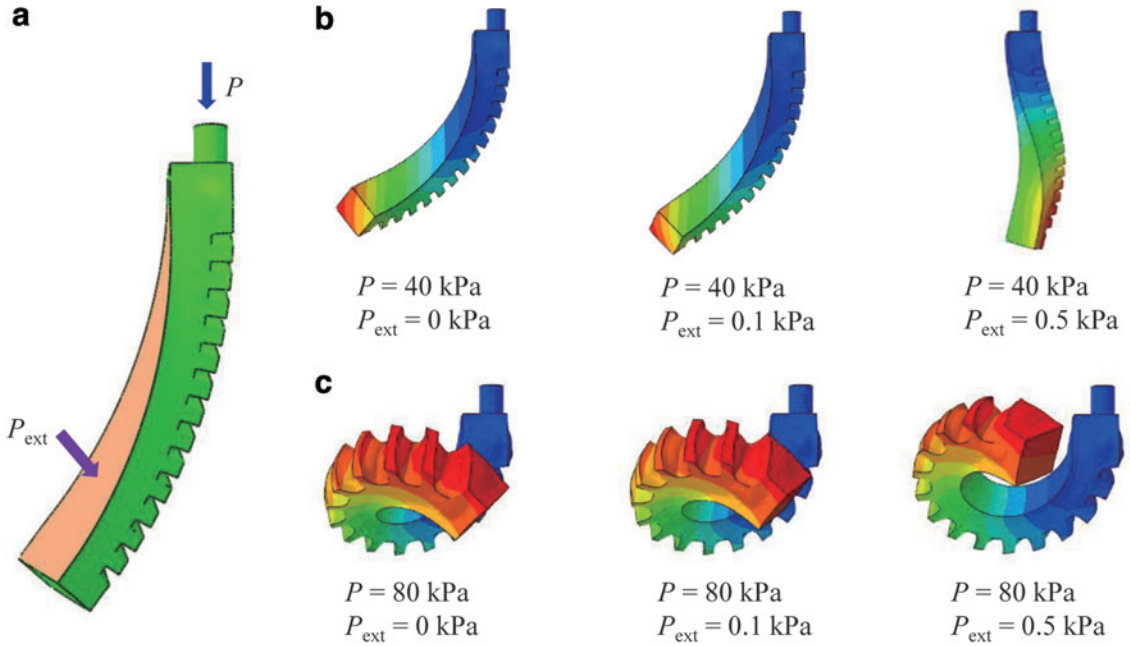

FIG. 8. FE results of the influence of external forces on the deformation of the gPNSAs. **(a)** An external pressure P_{ext} is applied on the bottom surface perpendicularly of a gPNSA with $\theta = 60°$. **(b)** FE results of the deformations of the gPNSA with various external pressure P_{ext} and the input pressure $P = 40$ kPa. **(c)** FE results of the deformations of the gPNSA with various external pressure P_{ext} and the input pressure $P = 80$ kPa. Color images are available online.

radius $R = 1/\kappa$ with the same boundary condition as in the experiments is described by the following parametrization:

$$\boldsymbol{X}_1(t) = \frac{P_t^2\pi^2 t + 4R^2 \sin t}{2\sqrt{4R^2 + P_t{}^2\pi^2}}, \tag{26}$$

$$\boldsymbol{X}_2(t) = \frac{P_t R\pi(t - \sin t)}{4R^2 + P_t^2\pi^2}, \tag{27}$$

$$\boldsymbol{X}_3(t) = R(-1 + \cos t). \tag{28}$$

The real coordinates of the points are fitted using the above function to obtain the experimental P_t and κ for each test using the least square method. Fitting examples are shown in Figure 5c and d. The experimental and fitted 3D space curves are compared in Figure 5e.

By using the procedures described above, the experimental κ and P_t are obtained for gPNSAs with various θ and P and compared with the theoretically predicted values, as shown in Figure 6. Both theoretical predictions (solid curves) and experimental results (markers) show that with the increase of the supplied pressures, curvatures linearly increase, while pitches decrease monotonically. When $\theta = 90°$, the gPNSA only has the bending deformation, leading to the zero of the pitch. Similar to the behaviors observed in Figure 4, small discrepancies between experiments and theoretical predictions exist at relatively larger θ, but they agree well at smaller ($\theta = 15°$) and very large ($\theta = 90°$).

Deformations with the gravity

In the theoretical model, we ignore gravity. To investigate the effect of the gravity on the developed model, the deformed shapes of the gPNSAs under the input pressure of $P = 60$ kPa are compared in three cases: (1) without gravity, (2) with gravity along the depth direction, and (3) with gravity along the length direction. The results are shown in Figure 7. It can be seen that the effect of gravity is not obvious on the deformation of the gPNSAs when fully inflated at $P = 60$ kPa. Thus, it is reasonable to neglect the gravity in the theoretical model for simplicity. It should be noted that based on the experimental observations and FE results, if the gPNSAs are not fully inflated, gravity significantly affects their deformation. It will be our future work to develop a more comprehensive model to characterize this effect.

Deformations with the external force

In this section, the effect of the external forces on the gPNSAs are also investigated. To study the deformed shape under external force, we use the FE simulations and select a gPNSA with $\theta = 60°$ as an illustration. In the simulation, the input pressure P and the external pressure P_{ext} will be applied, as shown in Figure 8a.

The deformed shapes of the gPNSA under various external pressure P_{ext} are shown in Figure 8b and c under input pressure $P = 40$ kPa and $P = 80$ kPa, respectively. The external force can be calculated as $F_{ext} = P_{ext} \times w_o \times l$. It should be noted that even when $P_{ext} = 0.1$ kPa, the generated force F_{ext} will be 0.156 N, which is comparable to the weight of the gPNSA (around 0.2 N). It can be observed that: (1) under the applied external pressure, the deformed shape is not a helical shape anymore, which is obvious for $P = 40$ kPa and $P_{ext} = 0.5$ kPa; (2) under the constant applied external pressure, the change of the deformed shape of the gPNSA under $P = 40$ kPa is larger than that under $P = 80$ kPa, indicating that the input pressure stiffens the gPNSA.

It should be noted that only a special case of applying uniformly distributed external pressure on the bottom surface is considered. The deformation of a gPNSA under an arbitrary external force is interesting but challenging, which will be our future work.

Model Analysis and Prediction for Design

In this section, we use the developed model to investigate the effects of geometrical parameters and material properties

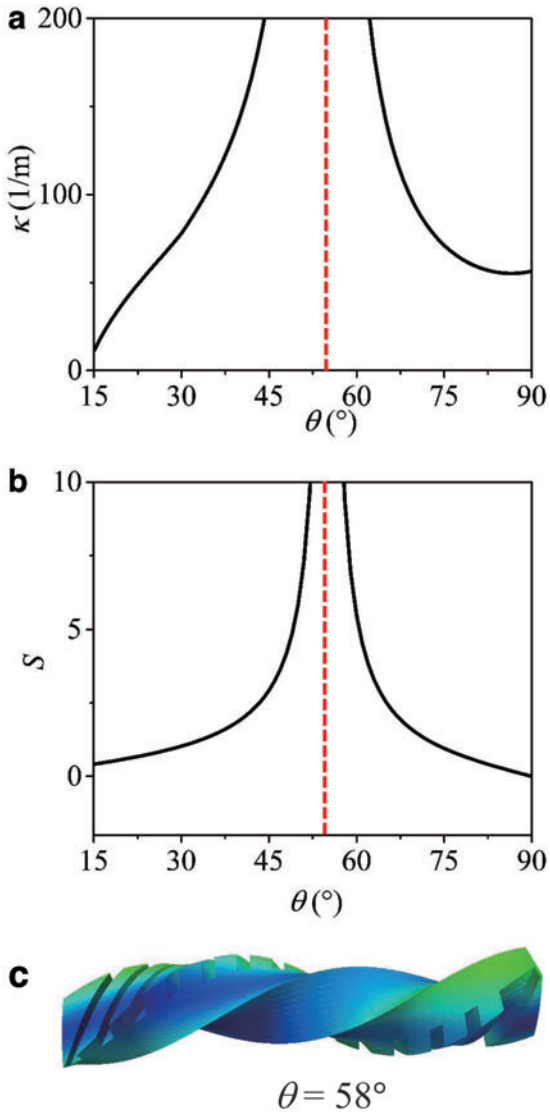

FIG. 9. Effects of the chamber angles θ on the curvature κ and slope S of gPNSAs. **(a)** κ is plotted as a function of the chamber angle θ. **(b)** S is plotted as a function of the chamber angle θ. **(c)** Illustration of theoretical deformation of a gPNSA with $\theta = 58°$. Color images are available online.

on the deformations of gPNSAs. It should be noted that the used model parameters are the same as those listed in Table 1, unless otherwise specified.

Effects of the chamber angles

As shown in Figures 3 and 4, there are some discrepancies between model-predicted deformations and experimental deformations with a relatively larger θ. To investigate this effect, we plot the curvature κ and slope ($S = P_t/[2\pi R]$) and of the gPNSA as a function of chamber angles θ as shown in Figure 9a and b, respectively.

From the figure, it can be seen that there is a critical transition angle $\theta_c \approx 55°$, where both slope and curvature go to infinity. It indicates that a gPNSA exhibits pure twisting motion around its centerline when $\theta = \theta_c$. For an illustration, we provide the model predicted results when $\theta = 58°$ as shown in Figure 9c, where the gPNSA shows mainly twisting motion. However, in practice, the chamber will be locally expanded and the large twisting is prevented by self-contact between the expanded surfaces of chambers, which is not considered in the current developed model.

It is worthy of mentioning that this effect of *critical angle* has already been well explored in the McKibben artificial muscles[29,30] and fiber-reinforced pneumatic soft actuators.[49,66] It is the first time to report this phenomenon in the pneu-net soft actuators. However, in this work, we mainly focus on first establishing a constitutive model of gPNSAs. Further investigation of the mechanism of this *critical angle* is useful as well but out the scope of this current work, which will be considered in our future work.

Effects of the inner chamber height

Besides the chamber angles θ, geometric parameters of the inner chambers are important in determining the deformations of gPNSAs. As shown in Figure 2b, the height h_3 is directly related to the generated force on the inner chambers. Therefore, we will investigate the influence of h_3 on the deformations of gPNSAs. For a comparison with the previous results in the Model Verification section, by varying the height of h_3, we keep that the total height of the chamber $h_2 + h_3$ is constant as 9 mm, while the other geometric parameters of the gPNSA are same as listed in Table 1 when the chamber angle θ is 30°.

Figure 10a shows the relation of the gPNSA curvatures κ with the height h_3 and the supplied pressures P. We can see that κ increases with the increase of h_3, which is reasonable because larger h_3 leads to larger inner surface areas and larger force.

To further verify the effectiveness of the developed model, we fabricate a new gPNSA with $h_3 = 4$ mm and $h_2 = 5$ mm. Figure 10b shows the gPNSA deformations of the model prediction and real-time experiment. The results demonstrate that the theoretical model successfully predicts the deformations of the gPNSA. Moreover, by comparing with the results of the original gPNSA with $h_3 = 7$ mm and

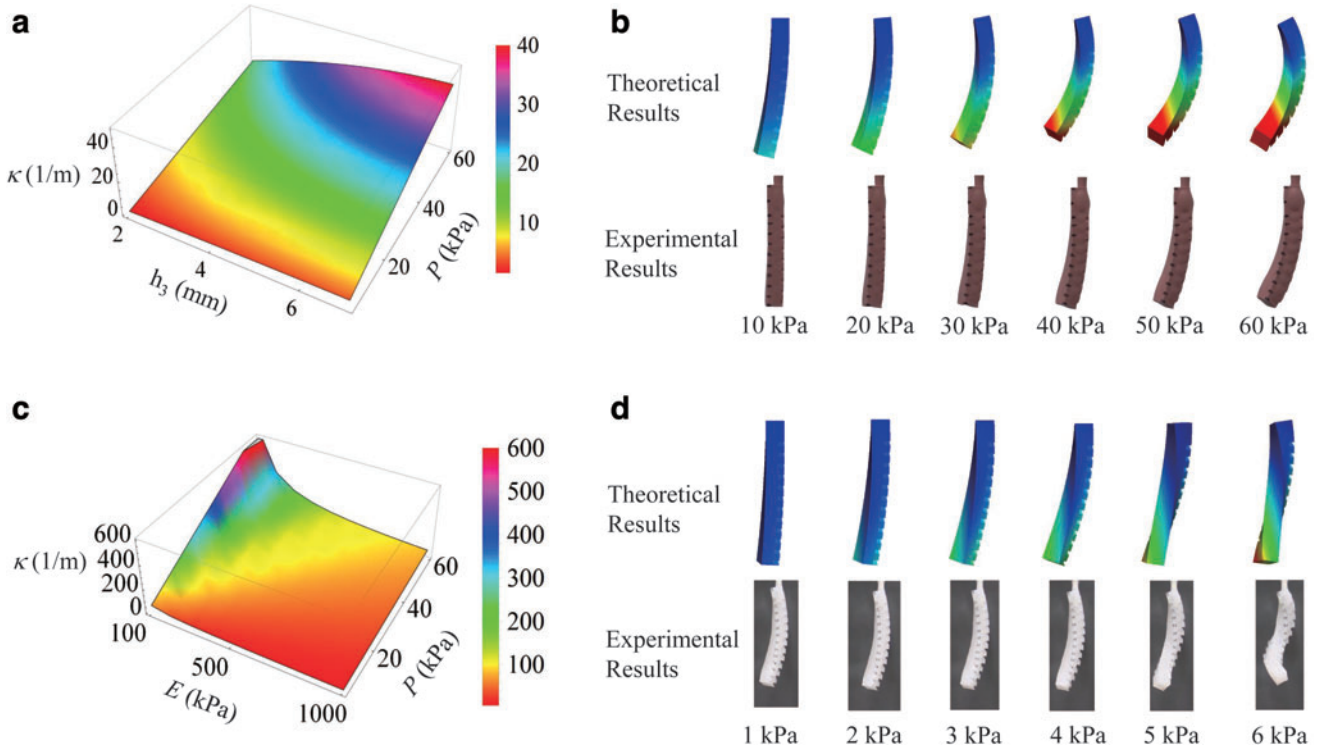

FIG. 10. Effects of the inner chamber height h_3 and Young's modulus E of the elastomers on the deformation of the gPNSA. **(a)** Theoretical prediction of the curvature κ of the deformed gPNSA as h_3 and the supplied pressure P changes. **(b)** Theoretical prediction and experimental validation of the gPNSA with $h_3 = 4$ mm and P varying from 10 to 60 kPa. **(c)** Theoretical prediction of the curvature κ of the deformed gPNSA as E and the supplied pressure P changes. **(d)** Theoretical prediction and experimental validation of the gPNSA made from Ecoflex 00-30 with P varying from 1 to 6 kPa. Color images are available online.

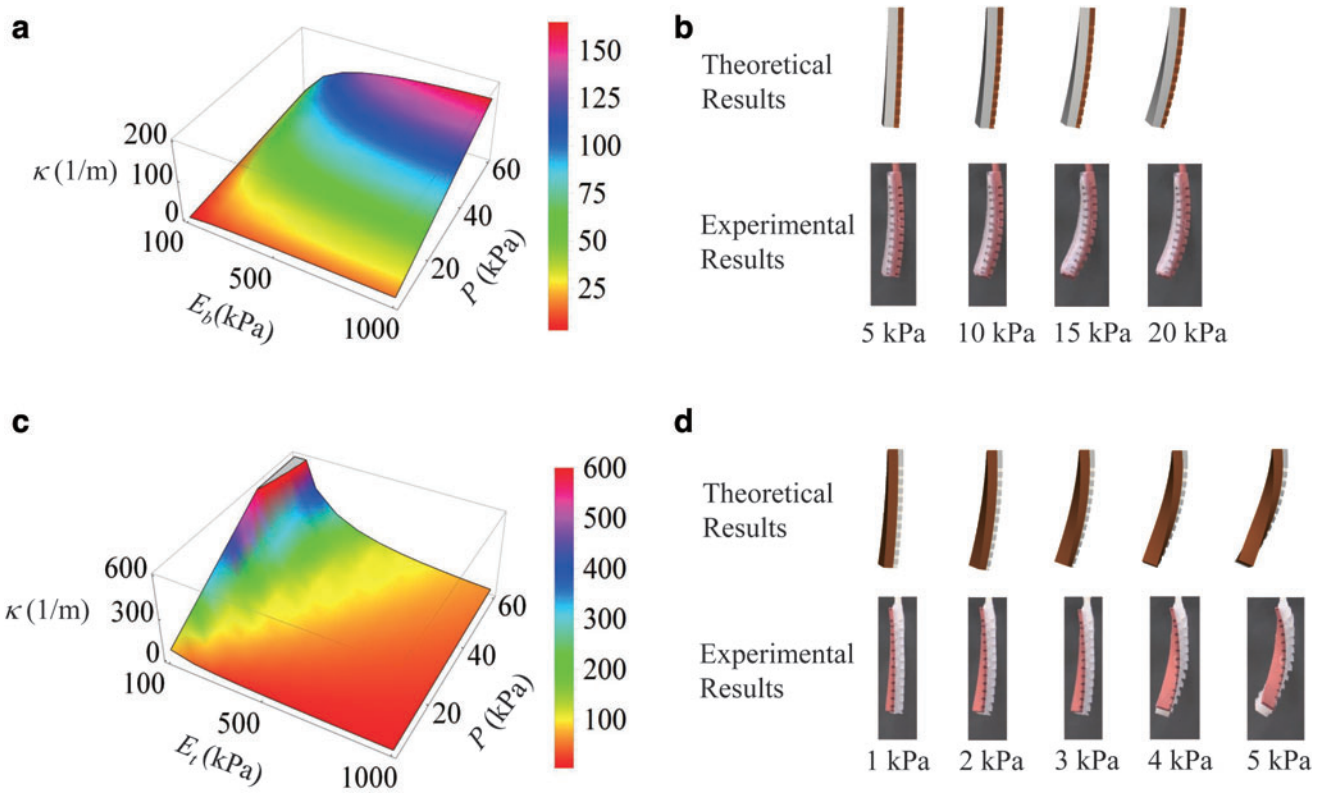

FIG. 11. Effects of Young's modulus E_b of the bottom layer and Young's modulus E_t of the top chamber layer on the deformation of the gPNSA. **(a)** Theoretical prediction of the curvature κ of the deformed gPNSA as E_b and the supplied pressure P changes. **(b)** Theoretical prediction and experimental validation of the gPNSA with the top chamber layer made from Elastosil M4601 and the bottom layer made from Ecoflex 00-30 with P varying from 5 to 20 kPa. **(c)** Theoretical prediction of the curvature κ of the deformed gPNSA as E_t and the supplied pressure P changes. **(d)** Theoretical prediction and experimental validation of the gPNSA with the top chamber layer made from Ecoflex 00-30 and the bottom layer made from Elastosil M4601 with P varying from 1 to 5 kPa. Color images are available online.

$P = 40$ kPa (Fig. 4b), this new gPNSA has relatively smaller bending and twisting due to its smaller chamber height h_3, which is the same as indicated in Figure 10a.

Effects of the material properties

Since our developed model is constitutive, it can be directly applied to gPNSAs with different elastomers by changing the material properties. Next, we will validate our developed model for gPNSAs made of elastomers with different Young's modulus E. Figure 10c shows the relation of the gPNSA curvatures with different Young's modulus E and the supplied pressures P. It can be observed that: (1) the curvature κ increases linearly with the increase of the supplied pressures P, same as the results in Figure 6a; (2) the curvature κ increases with the decrease of Young's modulus E. Therefore, we can know that the same deformation can be achieved at a relatively lower pressure if the material is softer.

For an illustration, we also fabricate a gPNSA made of a softer elastomer Ecoflex 00-30 (Young's modulus E of about 125 kPa).[67] Figure 10d shows the gPNSA deformations of the model prediction and real-time experiment, which demonstrates that the developed model can successfully predict the experimental results as well. Furthermore, we can see that the gPNSA with Ecoflex 00-30 (Young's modulus E of about 125 kPa) under $P = 6$ kPa can achieve the similar deformation as the gPNSA made from Elastosil M4601 (Young's modulus of about 483.5 kPa) under $P = 40$ kPa.

Model prediction with multiple elastomers

As a final demonstration, we validate our developed model by predicting gPNSAs with different elastomers in the top chamber layer and bottom layer, respectively (Fig. 1a).

In the first test, we change the materials of the bottom layer while keeping the material of the top chamber layer with Elastosil M4601 as used in the previous experiments. Figure 11a shows the relation of the gPNSA curvatures κ with different Young's modulus of the bottom materials E_b and the supplied pressures P. The results show that as Young's modulus of the bottom layer E_b decreases, the curvature κ of the gPNSA also decreases. As an example, we fabricate a gPNSA with the Ecoflex 00-30 as the bottom layer. Figure 11b shows the gPNSA results of the model prediction and experiments. It can be seen that the developed model well predicts the experimental results.

Another example of designing multiple-material gPNSA is shown in Figure 11c and d, where we change Young's modulus of the top chamber layer E_t while keeping the material of the layer chamber layer with Elastosil M4601 as

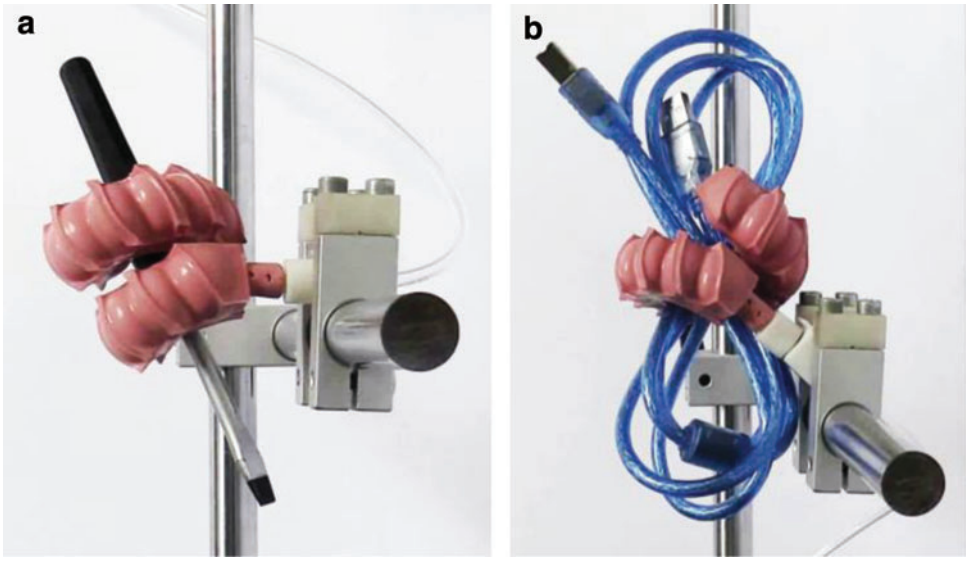

FIG. 12. Potential applications of a soft gripper using one gPNSA with $\theta = 60°$ to grasp the slender and irregularly shaped objects. Color images are available online.

used in the previous experiments. It can be observed that decreasing Young's modulus of the top chamber layer E_t leads to the increase of the deformation curvatures κ of gPNSAs. As shown in Figure 11d, a multiple-material gPNSA is also fabricated and tested, where the top chamber layer is made from Ecoflex 00-30 and the bottom layer is made from Elastosil M4601. The comparison results well demonstrate the effectiveness and generality of our developed constitutive model.

Conclusions

Based on the minimum potential energy method and the continuum rod theory, this article presents a constitutive modeling approach for gPNSAs with 3D deformations under single pneumatic actuation. We also conduct a series of experiments with different gPNSAs to verify the developed model. The proposed theoretical model can predict the deformed shapes directly from the geometrical parameters and applied pressures.

Comparing to the FE method, the current theoretical model is efficient, easy to be implemented, and the computational cost is low. By virtue of the analytical results, this model can also be directly applied to change the geometric and material parameters for designing a gPNSA with the desired deformation. Furthermore, the developed model is extended to analyze the deformation of the gPNSAs with multiple materials. The comparisons of the model-predicted results and the experimental results well demonstrate the effectiveness of our modeling approach. Due to the advantages of the helical deformations of gPNSAs in 3D space,[54,55] we can use one gPNSA (such as $\theta = 60°$) as a bionic soft gripper that can wind around the slender and irregularly shaped objects (Fig. 12). In the future, we will further extend this study for manipulating applications.

Author Disclosure Statement

No competing financial interests exist.

Funding Information

This work is supported by the National Natural Science Foundation of China (grant nos. 91848204, 91948302, and 51905336), and Shanghai Jiao Tong University Scientific and Technological Innovation Funds (grant no. 2019QYB08) and Innovative research team of high-level local universities in Shanghai.

References

1. Rus D, Tolley MT. Design, fabrication and control of soft robots. Nature 2015;521:467–475.
2. Laschi C, Mazzolai B, Cianchetti M. Soft robotics: technologies and systems pushing the boundaries of robot abilities. Sci Robot 2016;1:eaah3690.
3. Gu G, Zhu J, Zhu L, *et al.* A survey on dielectric elastomer actuators for soft robots. Bioinspir Biomim 2017;12:011003.
4. Majidi C. Soft robotics: a perspectivełcurrent trends and prospects for the future. Soft Robot 2014;1:5–11.
5. Gu G, Zou J, Zhao R, *et al.* Soft wall-climbing robots. Sci Robot 2018;3:eaat2874.
6. Umedachi T, Vikas V, Trimmer BA. Softworms: the design and control of non-pneumatic, 3D-printed, deformable robots. Bioinspir Biomim 2016;11:025001.
7. Shepherd RF, Ilievski F, Choi W, *et al.* Multigait soft robot. Proc Natl Acad Sci 2011;108:20400–20403.
8. Li T, Li G, Liang Y, *et al.* Fast-moving soft electronic fish. Sci Adv 2017;3:e1602045.
9. Marchese AD, Onal CD, Rus D. Autonomous soft robotic fish capable of escape maneuvers using fluidic elastomer actuators. Soft Robot 2014;1:75–87.
10. Della Santina C, Katzschmann RK, Bicchi A, *et al.* Model-based dynamic feedback control of a planar soft robot: trajectory tracking and interaction with the environment. Int J Robot Res 2020;39:490–513.
11. Marchese AD, Rus D. Design, kinematics, and control of a soft spatial fluidic elastomer manipulator. Int J Robot Res 2016;35:840–869.
12. Mazzolai B, Margheri L, Cianchetti M, *et al.* Soft-robotic arm inspired by the octopus: II. From artificial requirements to innovative technological solutions. Bioinspir Biomim 2012;7:025005.
13. Yi J, Chen X, Song C, *et al.* Customizable three-dimensional-printed origami soft robotic joint with effective behavior shaping for safe interactions. IEEE Trans Robot 2018;99:1–10.

14. Polygerinos P, Wang Z, Galloway K, *et al.* Soft robotic glove for combined assistance and at-home rehabilitation. Robot Auton Syst 2015;73:135–143.
15. Zhao H, O'Brien K, Li S, *et al.* Optoelectronically innervated soft prosthetic hand via stretchable optical waveguides. Sci Robot 2016;1:eaai7529.
16. Deimel R, Brock O. A novel type of compliant and underactuated robotic hand for dexterous grasping. Int J Robot Res 2016;35:161–185.
17. McEvoy MA, Correll N. Materials that couple sensing, actuation, computation, and communication. Science 2015; 347:1261689.
18. Trivedi D, Rahn CD, Kier WM, *et al.* Soft robotics: biological inspiration, state of the art, and future research. Appl Bion Biomech 2008;5:99–117.
19. Albu-Schäffer A, Eiberger O, Grebenstein M, *et al.* Soft robotics. IEEE Robot Autom Mag 2008;15:20–30.
20. Li X, Pan Y, Chen G, *et al.* Adaptive human-robot interaction control for robots driven by series elastic actuators. IEEE Trans Robot 2017;33:169–182.
21. Majidi C, Shepherd R, Kramer R, *et al.* Influence of surface traction on soft robot undulation. Int J Robot Res 2013;32: 1577–1584.
22. Whitesides GM. Soft Robotics. Angew Chem Int Ed 2018; 57:4258–4273.
23. Gorissen B, Reynaerts D, Konishi S, *et al.* Elastic inflatable actuators for soft robotic applications. Adv Mater 2017;29: 1604977.
24. Polygerinos P, Correll N, Morin SA, *et al.* Soft robotics: review of fluid-driven intrinsically soft devices; manufacturing, sensing, control, and applications in human-robot interaction. Adv Eng Mater 2017;19:1700016.
25. Ji X, Liu X, Cacucciolo V, *et al.* An autonomous untethered fast soft robotic insect driven by low-voltage dielectric elastomer actuators. Sci Robot 2019;4.
26. Sun JY, Zhao X, Illeperuma WRK, *et al.* Highly stretchable and tough hydrogels. Nature 2012;489:133–136.
27. Liu X, Liu J, Lin S, *et al.* Hydrogel machines. Mater Today 2020;36:102–124.
28. Polygerinos P, Wang Z, Overvelde J, *et al.* Modeling of soft fiber-reinforced bending actuators. IEEE Trans Robot 2015;31:778–789.
29. Bishop-Moser J, Kota S. Design and modeling of generalized fiber-reinforced pneumatic soft actuators. IEEE Trans Robot 2015;31:536–545.
30. Chou C, Hannaford B. Measurement and modeling of McKibben pneumatic artificial muscles. IEEE Trans Robot Autom 1996;12:90–102.
31. Davis S, Tsagarakis N, Canderle J, *et al.* Enhanced modelling and performance in braided pneumatic muscle actuators. Int J Robot Res 2003;22:213–227.
32. Ilievski F, Mazzeo AD, Shepherd RF, *et al.* Soft robotics for chemists. Angew Chem 2011;123:1930–1935.
33. Mosadegh B, Polygerinos P, Keplinger C, *et al.* Pneumatic networks for soft robotics that actuate rapidly. Adv Funct Mater 2014;24:2163–2170.
34. Tolley MT, Shepherd RF, Mosadegh B, *et al.* A resilient, untethered soft robot. Soft Robot 2014;1:213–223.
35. Deng Z, Stommel M, Xu W. A novel soft machine table for manipulation of delicate objects inspired by caterpillar locomotion. IEEE/ASME Trans Mechatr 2016;21:1702–1710.
36. Zhao H, Jalving J, Huang R, *et al.* A helping hand: soft orthosis with integrated optical strain sensors and EMG control. IEEE Robot Autom Mag 2016;23:55–64.
37. Yuk H, Zhang T, Parada GA, *et al.* Skin-inspired hydrogel-elastomer hybrids with robust interfaces and functional microstructures. Nat Commun 2016;7:12028.
38. Terryn S, Brancart J, Lefeber D, *et al.* Self-healing soft pneumatic robots. Sci Robot 2017;2:eaan4268.
39. Li Y, Chen Y, Yang Y, *et al.* Passive particle jamming and its stiffening of soft robotic grippers. IEEE Trans Robot 2017;33:446–455.
40. Hao Y, Wang T, Ren Z, *et al.* Modeling and experiments of a soft robotic gripper in amphibious environments. Int J Adv Robot Syst 2017;14:1–12.
41. Hao Y, Gong Z, Xie Z, *et al.* A soft bionic gripper with variable effective length. J Bionic Eng 2018;15:220–235.
42. Ge L, Dong L, Wang D, *et al.* A digital light processing 3D printer for fast and high-precision fabrication of soft pneumatic actuators. Sens Actuators A Phys 2018;273:285–292.
43. Zhang Y, Zhang N, Hingorani H, *et al.* Fast-response, stiffness-tunable soft actuator by hybrid multimaterial 3D printing. Adv Funct Mater 2019;29:1806698.
44. Chen X, Guo Y, Duanmu D, *et al.* Design and modeling of an extensible soft robotic arm. IEEE Robot Autom Lett 2019;4:4208–4215.
45. Bieze TM, Largilliere F, Kruszewski A, *et al.* Finite element method-based kinematics and closed-loop control of soft, continuum manipulators. Soft Robot 2018;5:348–364.
46. Gamus B, Salem L, Ben-Haim E, *et al.* Interaction between inertia, viscosity, and elasticity in soft robotic actuator with fluidic network. IEEE Trans Robot 2018;34: 81–90.
47. Garriga-Casanovas A, Collison I, Rodriguez y Baena F. Toward a common framework for the design of soft robotic manipulators with fluidic actuation. Soft Robot 2018;5: 622–649.
48. Ramachandran V, Majidi C. Deformation of microchannels embedded in an elastic medium. J Appl Mech 2018;85: 101004.
49. Connolly F, Walsh CJ, Bertoldi K. Automatic design of fiber-reinforced soft actuators for trajectory matching. Proc Natl Acad Sci 2017;114:51–56.
50. Felt W, Remy C. A closed-form kinematic model for fiber-reinforced elastomeric enclosures. J Mech Robot 2018;10: 014501.
51. Thomalla SD, Van de Ven JD. Modeling and implementation of the McKibben actuator in hydraulic systems. IEEE Trans Robot 2018:1–10.
52. Alici G, Canty T, Mutlu R, *et al.* Modeling and experimental evaluation of bending behavior of soft pneumatic actuators made of discrete actuation chambers. Soft Robot 2018;5:24–35.
53. de Payrebrune KM, O'Reilly OM. On constitutive relations for a rod-based model of a pneu-net bending actuator. Extreme Mech Lett 2016;8:38–46.
54. Wang T, Ge L, Gu G. Programmable design of soft pneu-net actuators with oblique chambers can generate coupled bending and twisting motions. Sens Actuators A Phys 2018; 271:131–138.
55. Ge L, Wang T, Zhang N, *et al.* Fabrication of soft pneumatic network actuators with oblique chambers. J Visual Exp 2018:e58277.
56. Hu W, Alici G. Bioinspired three-dimensional-printed helical soft pneumatic actuators and their characterization. Soft Robot2020;7:267–282.

57. Ogden RW. Non-linear Elastic Deformations. Chichester, UK: Ellis Horwood, 1984.
58. Holzapfel GA. Nonlinear solid mechanics: a continuum approach for engineering science. Meccanica 2002;37:489–490.
59. Chen Z, Majidi C, Srolovitz DJ, *et al.* Tunable helical ribbons. Appl Phys Lett 2011;98:011906.
60. Wang D, Li L, Serjouei A, *et al.* Controllable helical deformations on printed anisotropic composite soft actuators. Appl Phys Lett 2018;112:181905.
61. Reddy JN. An Introduction to Continuum Mechanics. Cambridge, UK: Cambridge University Press, 2013.
62. de Payrebrune KM, O'Reilly OM. On the development of rod-based models for pneumatically actuated soft robot arms: a five-parameter constitutive relation. Int J Solids Struct 2017;120:226–235.
63. Antman SS. The theory of rods. In: Truesdell C. (Eds). Linear Theories of Elasticity and Thermoelasticity. Berlin, Heidelberg: Springer, 1973, pp. 641–703.
64. Ahrens J, Geveci B, Law C. Paraview: An End-User Tool for Large Data Visualization. In: Hansen CD, Johnson CR. (Eds). The Visualization Handbook. Oxford, UK: Butterworth-Heinemann, 2005, pp. 717–731.
65. Schneider CA, Rasband WS, Eliceiri KW. NIH Image to ImageJ: 25 years of image analysis. Nat Methods 2012;9: 671–675.
66. Wang B, Mcdaid A, Biglari-Abhari M, *et al.* A bimorph pneumatic bending actuator by control of fiber braiding angle. Sens Actuators A Phys 2017;257:173–184.
67. Shintake J, Sonar H, Piskarev E, et al. Soft pneumatic gelatin actuator for edible robotics. In 2017 IEEE/RSJ International Conference on Intelligent Robots and Systems (IROS), Vancouver, BC, Canada: IEEE, 2017, pp. 6221–6226.

Address correspondence to:
Guoying Gu
Robotics Institute
School of Mechanical Engineering
Shanghai Jiao Tong University
Shanghai 200240
China

E-mail: guguoying@sjtu.edu.cn